



PAPER

Electrode configuration study for three-dimensional imaging of on-chip ECT

To cite this article: Xian Feng Hor *et al* 2023 *Eng. Res. Express* **5** 025003

View the [article online](#) for updates and enhancements.

You may also like

- [Fringe effect of electrical capacitance and resistance tomography sensors](#)
Jiangtao Sun and Wuqiang Yang
- [3D image reconstruction using an ECT sensor with a single layer of electrodes](#)
Jingjing Shen, Shuanghe Meng, Mao Ye *et al.*
- [ECT in a large scale industrial pneumatic conveying system](#)
M Neumayer, T Bretterkieber, T Suppan *et al.*

Engineering Research Express



PAPER

Electrode configuration study for three-dimensional imaging of on-chip ECT

RECEIVED
22 November 2022

REVISED
19 February 2023

ACCEPTED FOR PUBLICATION
16 March 2023

PUBLISHED
6 April 2023

Xian Feng Hor¹ , Pei Ling Leow^{1,*} , Mohamed Sultan Mohamed Ali¹ , Pei Song Chee² ,
Shahrulnizahani Mohammad Din¹  and Wen Pin Gooi¹ 

¹ Faculty of Electrical Engineering, Universiti Teknologi Malaysia, 81310 Skudai, Johor, Malaysia

² Department of Mechatronics and Biomedical Engineering, Lee Kong Chian Faculty of Engineering and Science, Universiti Tunku Abdul Rahman, 43000 Kajang, Selangor, Malaysia

* Author to whom any correspondence should be addressed.

E-mail: leowpl@utm.my

Keywords: electrode design, on-chip ECT, three-dimensional imaging

Abstract

Conventional electrical capacitance tomography (ECT) is widely used for monitoring the fluids flow in a pipeline. As the emergence of microfluidics, the tomography system has been miniaturized and integrated into the microfluidic platform for imaging purposes. The on-chip ECT is designed to monitor the permittivity distribution of the micro-platform by integrating the planar electrodes with the sensing region. However, limited research has been reported on the electrode design of on-chip ECT, especially for three-dimensional imaging. Thus, this study investigated the electrode design of an on-chip ECT that is capable for image reconstruction in three-dimensions. Four different electrode configurations with different numbers of electrode and arrangements are investigated by simulation to determine the appropriate configuration for three-dimensional imaging. The electrode dimension is optimized based on the sensitivity distribution using the sensitivity variation parameter (SVP). The simulation results shows that the electrode configuration with dual sensing planes enable three-dimensional imaging. The central electrode of each sensing plane is crucial for restoring a floating object. In experiment, the imaging object that was positioned at different vertical and horizontal locations was reconstructed successfully with an average correlation coefficient of 0.4370 using linear back projection (LBP) algorithm. This work has disclosed the appropriate electrode configuration for the three-dimensional imaging of an on-chip ECT system.

1. Introduction

Electrical capacitance tomography (ECT) system reconstructs images based on the permittivity distribution of a sensing area. The capacitance measurement is accomplished by inducing voltages at the boundary electrodes. Thus, the ECT system is advantageous for monitoring the fluids that exhibits dielectric properties. It has been applied in the monitoring the jet flame within combustion can [1], the water-oil multiphase flow [2, 3], the fluidized beds flow [4], and the oil-gas pipe flow [5]. The ECT system can distinguish different flow patterns, including the stratified pattern, the core pattern, and the annular pattern [6] using an image reconstruction algorithm. Numerous researches have been focused on the image reconstruction algorithms [7–9]. The studies on the electrode design, however, are limited. One of the efforts shown in [10] had investigated the electrode number, the electrode length, the external or internal electrode, the Earth screen, and the driven guard electrode. However, it was limited to two-dimensional imaging of an pipeline application. A single sensing plane is normally employed for two-dimensional imaging. In contrast, more sensing planes are required for three-dimensional imaging. For instance, [11, 12] reported that three sensing planes, with 12 electrodes in each plane, were used to reconstruct three-dimensional images of flowing fluids within a conduit. These three sensing planes were equally arranged in the axial direction of the pipeline to distribute the electric fields homogeneously over the volumetric space. The electric fields needed to enclose the sensing domain all over the directions to

produce the necessary sensitivity distribution for the three-dimensional imaging. Thus, the design of electrode configuration is important in reconstructing three-dimensional images with good quality.

As the emergence of the lab-on-chip, tomography has been integrated into microfluidics platform. For instance, the on-chip electrical impedance tomography (EIT) was designed for imaging the multi-nuclear single cellular organism of *Physarum Polycephalum* in two-dimensions [13, 14]. The design used a single sensing plane with 16 peripheral planar electrodes to capture the impedance signals. By adopting this planar electrode structure, the ECT was shrunk down for imaging the fluids and cell cultures on a microplatform. For example, using the on-chip ECT, the stagnant and flowing fluids within the microchamber were imaged successfully by mounting single sensing plane with 8 planar electrodes to the bottom of the microchamber [15]. Although the flowing regime was indicated properly, the images were limited to two-dimensions and the depth information could not be provided. As compared to fluidics imaging, three-dimensional imaging is desired for visualizing the cell culture. This is because culturing the cells using a 3D model can provide a more realistic environment than the traditional 2D cell culture that cultivates cells on a flat substrate [16]. Thus, the on-chip ECT with three-dimensional imaging ability can be used to observe the morphology of 3D cell culture. The variation of electrical signal can be used to monitor the cell adhesion, migration, spreading, and proliferation in the cell cycle process or cell-drug [17–20]. For instance, by taking the electrical signal before the drug test as the reference point, the subsequent changes of electrical signal can be profiling for the monitoring of drug test [16]. Thus, the idea of using two sensing planes was presented by [21] to achieve the three-dimensional imaging of *Saccharomyces Cerevisiae* cells that were encapsulated within an agar gel. The two sensing planes were attached to the top and bottom of the sensing region of microchamber. However, the image quality is less satisfactory, as the reconstructed images were constrained to regional restoration. Moreover, there is a lack of studies investigating on how the electrode design affects the imaging performance of an on-chip ECT. Therefore, it is desirable to discover the appropriate electrode design for three-dimensional imaging of an on-chip ECT system to expand its functionality and application in monitoring the cell cultures. Although the spatial resolution of on-chip ECT is not comparable to the electron microscopes, the ECT is harmless, label free, real time, portable, and low cost. To bridge this gap, this paper studies a series of different planar electrode designs for the imaging of an on-chip ECT in three-dimensions. Based on a modelling approach, the ways of different electrode designs in influencing the imaging performance are investigated. The final design, which could reconstruct images in three-dimensions, are validated experimentally. The results are analyzed and discussed in detail.

2. COMSOL multiphysics modelling

2.1. On-chip ECT

The forward problem of an ECT system is to solve the capacitance based on the defined permittivity distribution. The forward problem can be illustrated mathematically as

$$C = -\frac{1}{V} \oint_s \varepsilon(\mathbf{r}) \nabla_{\varnothing}(\mathbf{r}) dS, \quad (1)$$

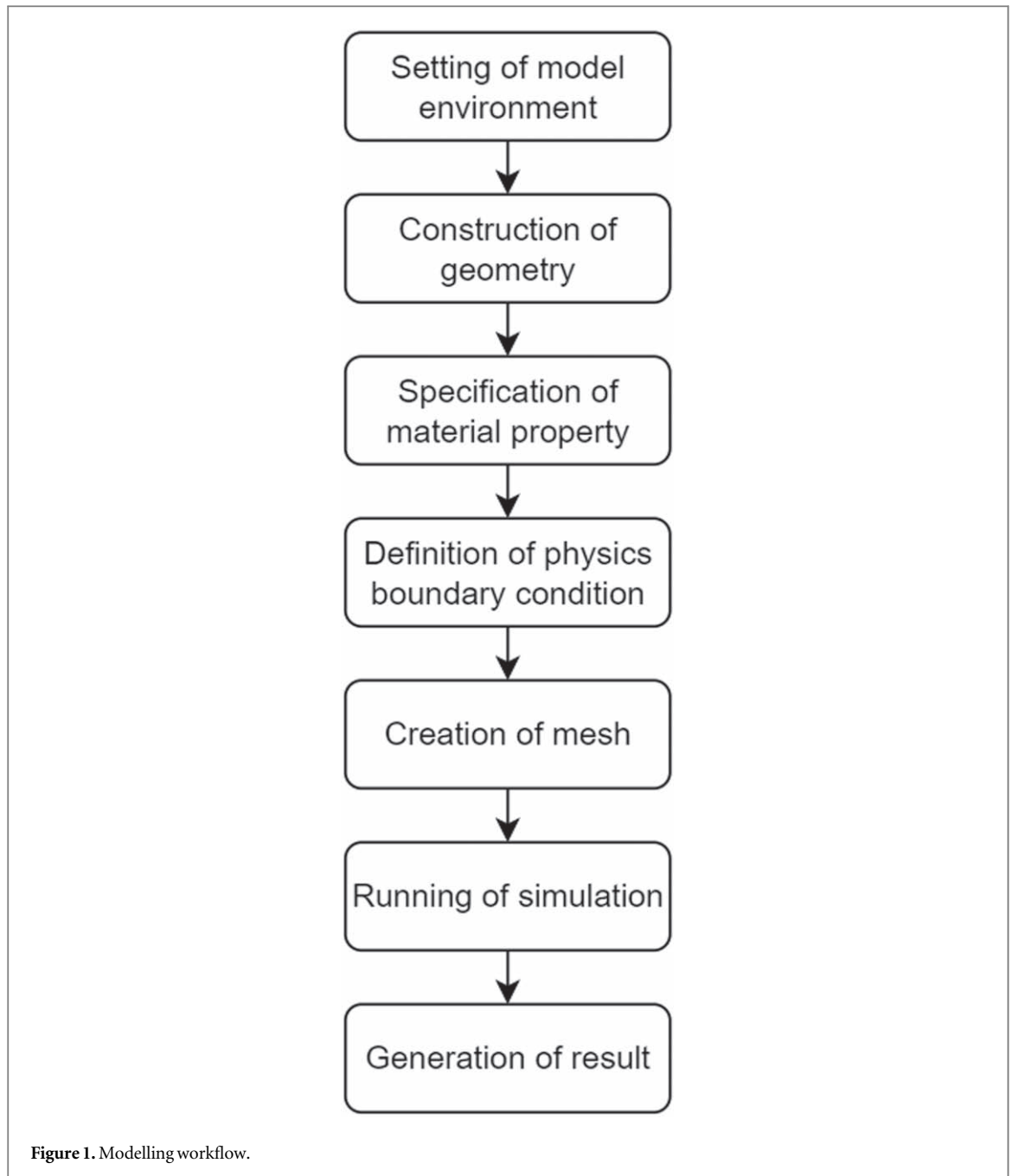
where C is the measured capacitance, V is the applied voltage, $\oint_s dS$ is the closed surface derivation, $\varepsilon(\mathbf{r})$ is the spatial permittivity distribution, and $\varnothing(\mathbf{r})$ is the potential difference. To solve this forward problem, this work conducted numerical modelling using a simulation software, COMSOL Multiphysics (version 5.4). The flow of modelling is depicted in figure 1.

A three-dimensional model was set up in the electrostatics module. The electrostatic module was selected, as no wave effect was induced by the low-frequency excitation signal from the ECT when measuring the capacitance [22]. Subsequently, the geometry of the on-chip ECT was created, and its material property was defined. In this study, the sensing region of the microchamber was 3 mm in height and 10 mm in diameter. The boundary electrodes were defined with an applied voltage value. For an electrode pair, the excitation electrode was set at 1 V (default value) and the sensing electrode was grounded. Subsequently, mesh with normal resolution was generated to discretize the complicated geometry model into many small parts. The simulation was eventually executed to compute the capacitance using the finite element method. The simulation was carried out using a conventional computer, which was equipped with the i5-7300HQ processor, 8GB 2666MHz random-access memory, and GTX 1050 graphics processing unit.

2.2. Three-dimensional image reconstruction

The images were reconstructed by LBP algorithm, which is formulated as

$$g(x, y, z) = \frac{\sum_{i=1}^m \lambda_i S_i(x, y, z)}{\sum_{i=1}^m S_i(x, y, z)} \quad (2)$$



where $g(x, y, z)$ is the grey level at coordinate (x, y, z) , λ_i is the normalized capacitance of electrode pair i , $S_i(x, y, z)$ is the sensitivity map of an electrode pair i at the coordinate of (x, y, z) , m is the total number of possible electrode pair combinations. Using the single excitation sensing protocol, with p number of electrodes, the number of possible electrode pair combinations, m in equation (2) is equal to $p \times (p - 1) \times 0.5$ [23].

The sensitivity map of an electrode pair i , $S_i(x, y, z)$ in equation (2) is calculated using the electric field as

$$S_i(x, y, z) = -\frac{1}{V_a V_b} \int_{V(x,y,z)} E_a(x, y, z) \cdot E_b(x, y, z) dx dy dz \quad (3)$$

Referring equation (3), the sensitivity map for an electrode pair i is the dot product of the electric field E_a and E_b , at an applied voltage V_a and V_b , respectively. The electrode pair i is made up by electrode a and electrode b . When generating the sensitivity map, the air is defined as the background material. Comparing to other materials, the sensitivity map performs better with the air as the background material [24].

The normalized capacitance, λ_i in equation (2) is calculated as

$$\lambda_i = \frac{C_i - C_{i(\text{low})}}{C_{i(\text{high})} - C_{i(\text{low})}} \quad (4)$$

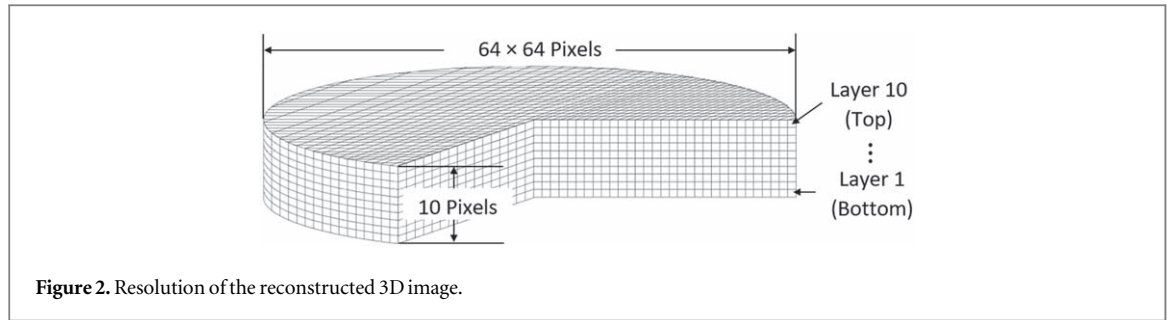


Figure 2. Resolution of the reconstructed 3D image.

where C_i is the measured capacitance of an electrode pair i , $C_{i(\text{low})}$ is the capacitance of an electrode pair i when the sensing region is filled with the lowest permittivity material, $C_{i(\text{high})}$ is the capacitance of electrode pair i when the sensing region is filled with the highest permittivity material. In this work, the lowest permittivity material is the agar gel, whereas the highest permittivity material is the agar gel with the encapsulated *Saccharomyces Cerevisiae*.

The LBP algorithm in equation (2) normalizes the greyscale level $g(x, y, z)$ into the range between 0 to 1. The greyscale level $g(x, y, z)$ is volumetric data, in which every voxel is assigned with an intensity value. Therefore, to provide a vivid visualization, the iso-surface of the 90% highest intensity value is plotted. The three-dimensional images were reconstructed with the resolution of $64 \times 64 \times 10$ pixels, as depicted in figure 2. The horizontal X-Y resolution is 64×64 pixels, while the vertical Z resolution is 10 pixels. Consequently, the total number of reconstructed pixels is 40960. Both the LBP algorithm computation as well as the iso-surface visualization were completed using the MATLAB (version R2018b).

2.3. Imaging quality assessment

The quality of reconstructed images is evaluated quantitatively using the correlation coefficient. The correlation coefficient is defined as

$$CC = \frac{\sum_{t=1}^w (g_t - \bar{g})(\hat{g}_t - \bar{\hat{g}})}{\sqrt{\sum_{t=1}^w (g_t - \bar{g})^2 (\hat{g}_t - \bar{\hat{g}})^2}} \quad (5)$$

where g_t and \hat{g}_t represent the true permittivity and the reconstructed permittivity at the t th pixel, respectively. The \bar{g} and $\bar{\hat{g}}$ denote the mean of the true permittivity and the reconstructed permittivity, respectively. Meanwhile, the w is the total number of pixels. The correlation coefficient examines the degree of association between the true permittivity and the reconstructed permittivity. The range of correlation coefficient is between -1 to 1 , where -1 shows a perfect negative relationship, 1 denotes a perfect positive relationship, and 0 shows no relationship. Therefore, the closer the correlation coefficient to the value of 1 , the higher the quality of the reconstructed image.

3. Numerical investigation and results

3.1. Electrode configuration for the three-dimensional imaging on-chip ECT

Four different electrode configurations listed in table 1 were investigated for three-dimensional imaging. Their respective volumetric sensitivity distribution is calculated by summing the sensitivity map of each electrode pair in equation (3). The intensity of the sensitivity is scaled into the range from 0 to 1. The closer the intensity to the value of 1, the higher the sensitivity to the capacitance changes. Configuration I had a single sensing plane attached to the bottom of the sensing region with 8 peripheral electrodes. According [10], the electrode number is usually either 8 or 12. However, the sensitivity of configuration I is concentrated around the electrode region. To generate a more uniform sensitivity at the bottom region, configuration II increased the electrode number to 16. However, the sensitivity is weak at the top region, as for configurations I and II, the sensing plane is only attached at the bottom. Therefore, another sensing plane is placed at the top for configurations III and IV. As compared to configuration III, configuration IV presented better sensitivity in the center region with the extra central electrodes on both the top and bottom planes.

The peripheral electrode and central electrode are labelled in figure 3. The peripheral electrode refers to the planar electrode surrounding the sensing region, whereas the central electrode refers to the planar electrode at the center of the sensing region. The length and width of the peripheral electrode were 1.2 mm and 0.6 mm, respectively, meanwhile the diameter of the central electrode is 0.4 mm [25].

To examine the imaging ability, an imaging cubic object is used. The imaging object is placed across different horizontal and vertical positions as illustrated in figure 4. The size of the imaging object is $1 \text{ mm} \times$

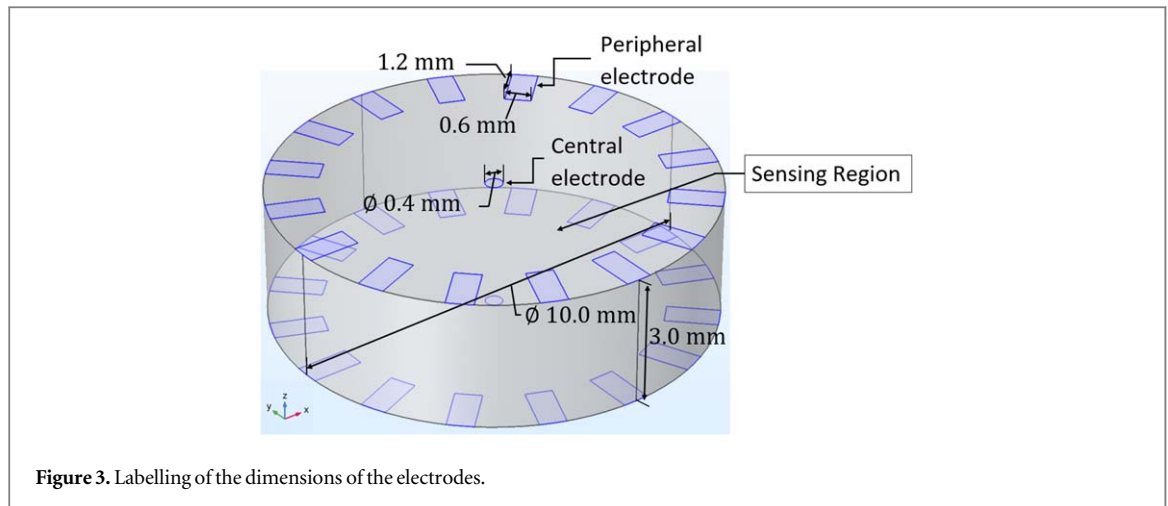
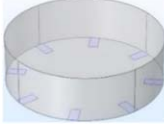

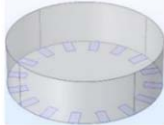

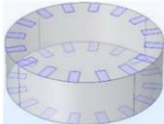

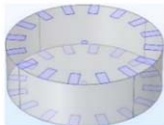




Figure 3. Labelling of the dimensions of the electrodes.

Table 1. Four different electrode configurations.

No.	Description	Electrodes Configuration	Sensitivity Distribution
I	Bottom sensing plane with 8 peripheral electrodes		
II	Bottom sensing plane with 16 peripheral electrodes		
III	Top and bottom sensing planes, each plane consists 16 peripheral electrodes		
IV	Top and bottom sensing planes, each plane consists 16 peripheral electrodes and a central electrode		



Intensity Scale Bar

1 mm × 1 mm (length × width × height). In the experiment, the imaging object was created by encapsulating the yeast cells within the cubic agar gel. Although the absolute permittivity of yeast and its culturing agar are yet to be known, the permittivity value of the cubic imaging object and its surrounding in the simulation study were set to the value of 3 and 1, respectively, as referring the experimental results of [14], the capacitance ratio of yeast towards its culturing agar was 3 : 1. The simulation results are tabulated in table 2.

The results in table 2 show that configuration I can reconstruct the object at positions P3 and P4, which wear near to the peripheral electrodes. The result proved that the sensitivity of configuration I was constrained to the electrode region. Compared to configuration I, configuration II can locate the imaging object at the bottom of the sensing region, which were at positions P1, P2, P3, and P4. Due to the increment of electrode number, configuration II had more independent measurement combinations and thus presented a more homogeneous sensitivity distribution at the bottom region. Whereas, configuration III with dual sensing planes successfully located the imaging object at position P6, which was at the top of the sensing region. The success of locating the object at position P6 was due to the strengthen of sensitivity at the top region by adding a top sensing plane. Moreover, the quality of reconstructed imaging object by configuration III at positions P1, P2, P3 and P4 were improved. By adding a central electrode to each sensing plane, configuration IV successfully reconstructed the imaging object at all six different positions, including the floating position P5, as the sensitivity of the central

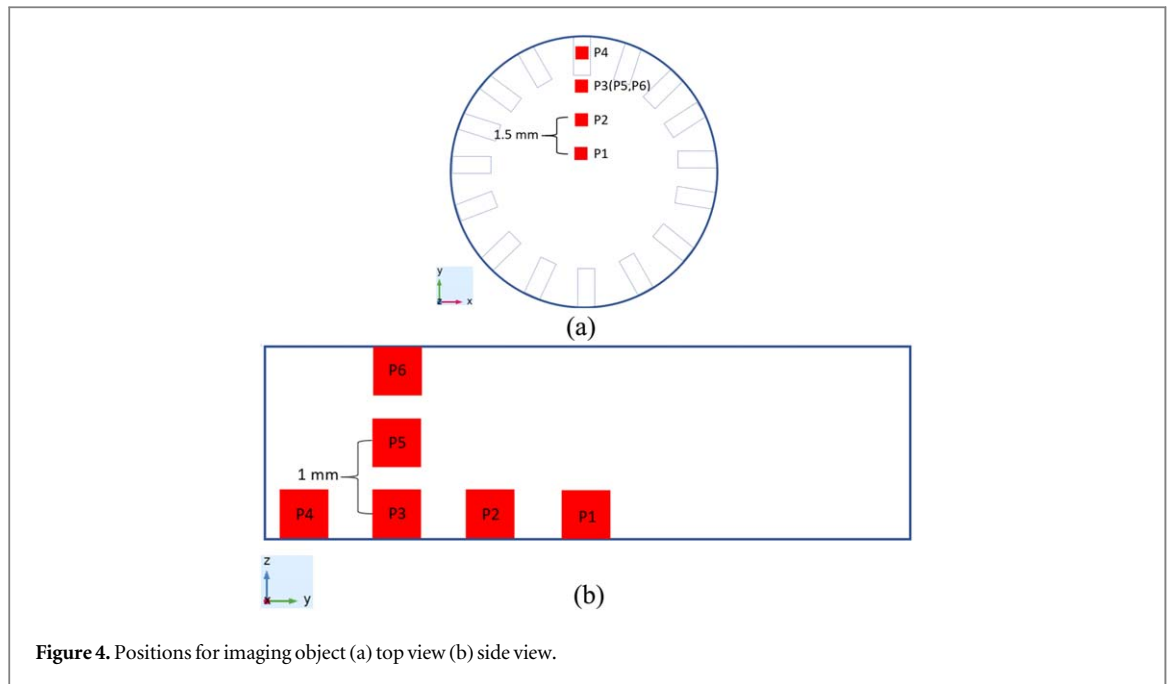


Figure 4. Positions for imaging object (a) top view (b) side view.

Table 2. Simulation results of four different electrode configurations.

Position	Configuration I	Configuration II	Configuration III	Configuration IV
P1				
P2				
P3				
P4				
P5				
P6				

region was strengthened. Configuration IV indicated that attaching the central electrode was critical to enhance the sensitivity for three dimensional imaging, especially in restoring a floating object.

The overall result shows that, for three-dimensional imaging, a uniform and homogeneous sensitivity distribution is significant in reconstructing the imaging object at different spatial positions. The desired sensitivity distribution can be generated by employing configuration IV for an on-chip ECT, as indicated by the simulation results in table 2. Since configuration IV performed the best, configuration IV is employed for the following studies.

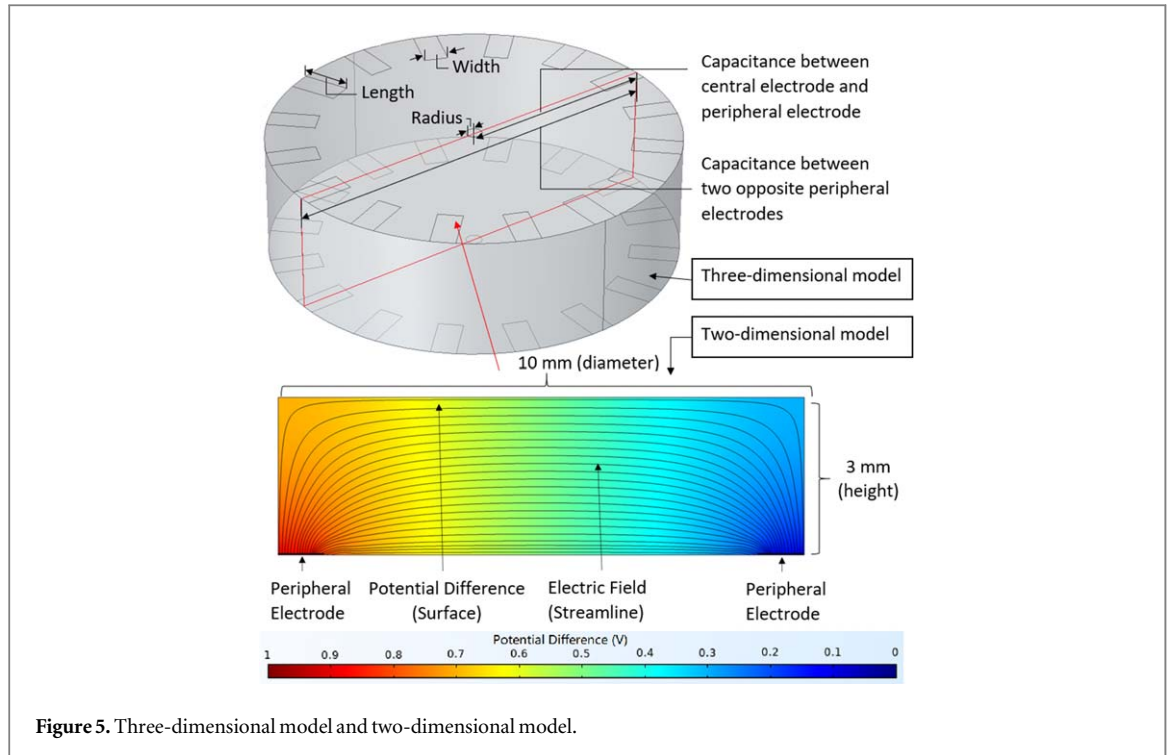


Figure 5. Three-dimensional model and two-dimensional model.

3.2.3.2 Sensitivity variation parameter (SVP) to optimize electrode dimension

In this section, the electrode dimension of configuration IV is optimized based on the homogeneity of sensitivity distribution. According to [26], a homogeneous sensitivity distribution produces smooth images with fewer spikes. To evaluate the homogeneity of sensitivity distribution, adopting the concept of standard deviation and coefficient of variant, the sensitivity variation parameter (SVP) is proposed by [26] and is defined as:

$$SVP = \frac{S_{dev}}{S_{avg}} \quad (6)$$

where

$$S_{avg} = \frac{1}{X \times Y \times Z} \sum_{x=1}^X \sum_{y=1}^Y \sum_{z=1}^Z S(x, y, z) \quad (7)$$

$$S_{dev} = \left(\frac{1}{X \times Y \times Z} \sum_{x=1}^X \sum_{y=1}^Y \sum_{z=1}^Z (S(x, y, z) - S_{avg})^2 \right)^{1/2} \quad (8)$$

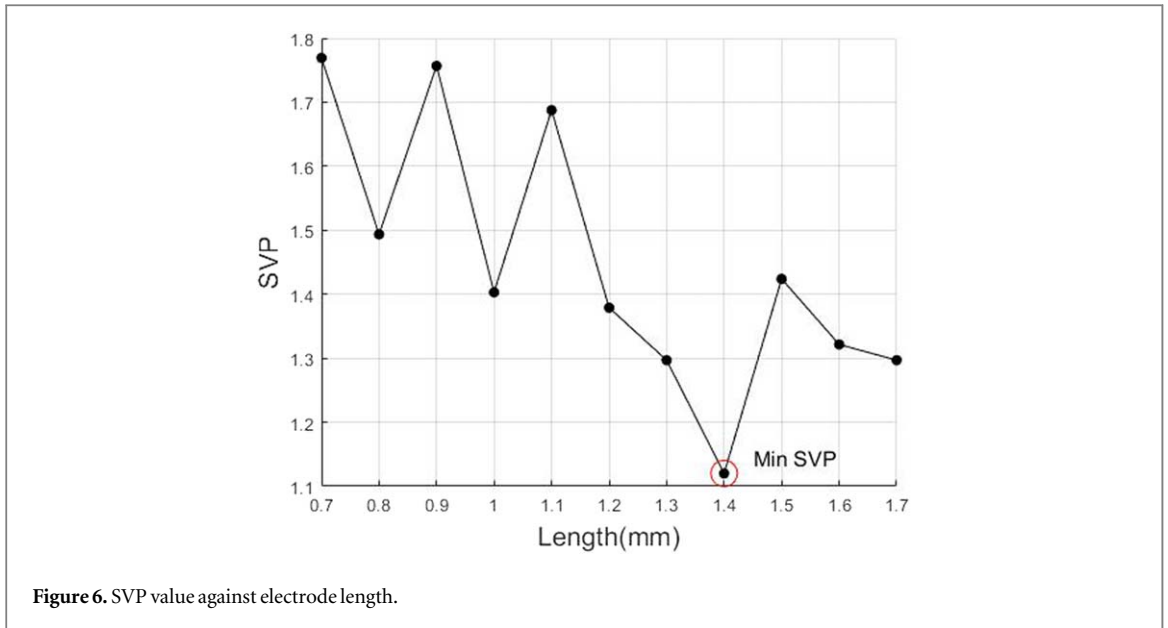
and

$$S(x, y, z) = \sum_{i=1}^m S_i(x, y, z) \quad (9)$$

S_{avg} in equation (7) refers to the average intensity of the sensitivity distribution, and S_{dev} in equation (8) is the positive square root of the variance of the intensity at coordinate (x, y, z) from the average intensity, S_{avg} . Whereas, $S(x, y, z)$ in equation (9) is the overall sum of the sensitivity distribution of each electrode pair. Based on the calculation of the SVP in equation (6), the smaller the SVP magnitude, the more homogeneous the sensitivity distribution. As the result, the electrode dimension with the smaller SVP value is preferred since it generates less variation in the sensitivity distribution.

Three electrode dimensions were to be defined: the length of the peripheral electrode, the width of the peripheral electrode, and the radius of the central electrode. These three-dimensions are labelled in figure 5.

The length of the peripheral electrode was first defined using the two-dimensional model illustrated in figure 5. The two-dimensional model involved the peripheral electrode at the bottom to ensure a strong generation of electrical signal across the sensing region during the SVP evaluation. A series of peripheral electrode length from 0.7 mm to 1.7 mm, with a 0.1 mm step size, were investigated. The SVP result is plotted in figure 6. The result in figure 6 shows that the electrode length of 1.4 mm had the minimum SVP value of 1.1285. Therefore, 1.4 mm was chosen as the length of the peripheral electrode, as the 1.4 mm generated the least variation in sensitivity distribution with the smallest SVP value.



Subsequently, based on the defined peripheral electrode length of 1.4 mm, the peripheral electrode width and the central electrode radius were identified using the three-dimensional model shown in figure 5. During the identification, the sensing strength between two opposite electrodes is equaled to the sensing strength between a central electrode to a peripheral electrode. To equal the sensing strength, the capacitance between two opposite electrodes, C_{p-p} is approximated to the capacitance between a central electrode to a peripheral electrode, C_{c-p} . The approximation is mathematically expressed as

$$C_{p-p} = C_{c-p} \quad (10)$$

$$\frac{\varepsilon A_p}{d_{p-p}} = \frac{\varepsilon A_c}{d_{c-p}} \quad (11)$$

$$\frac{\varepsilon A_p}{d_{p-p}} = \frac{2 \times \varepsilon A_c}{d_{p-p}} \quad (12)$$

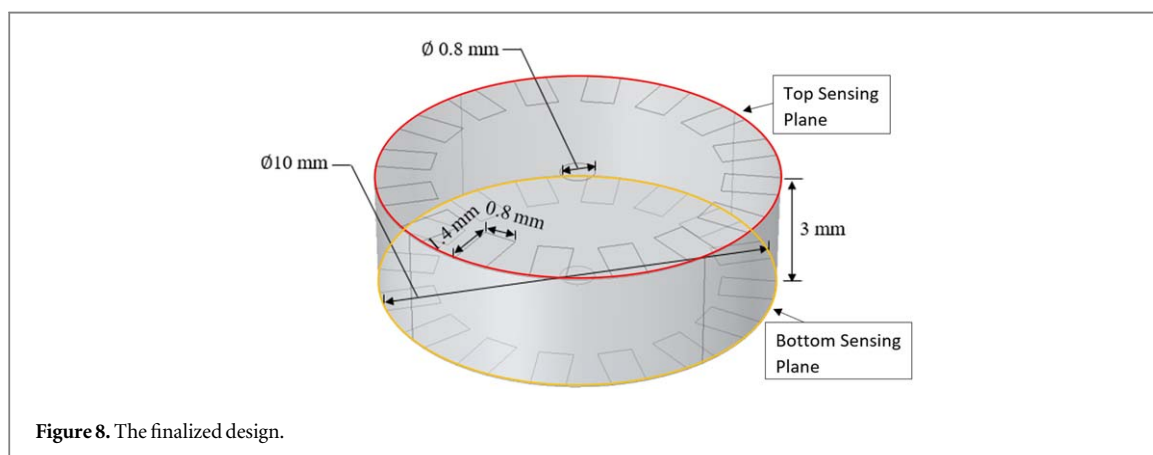
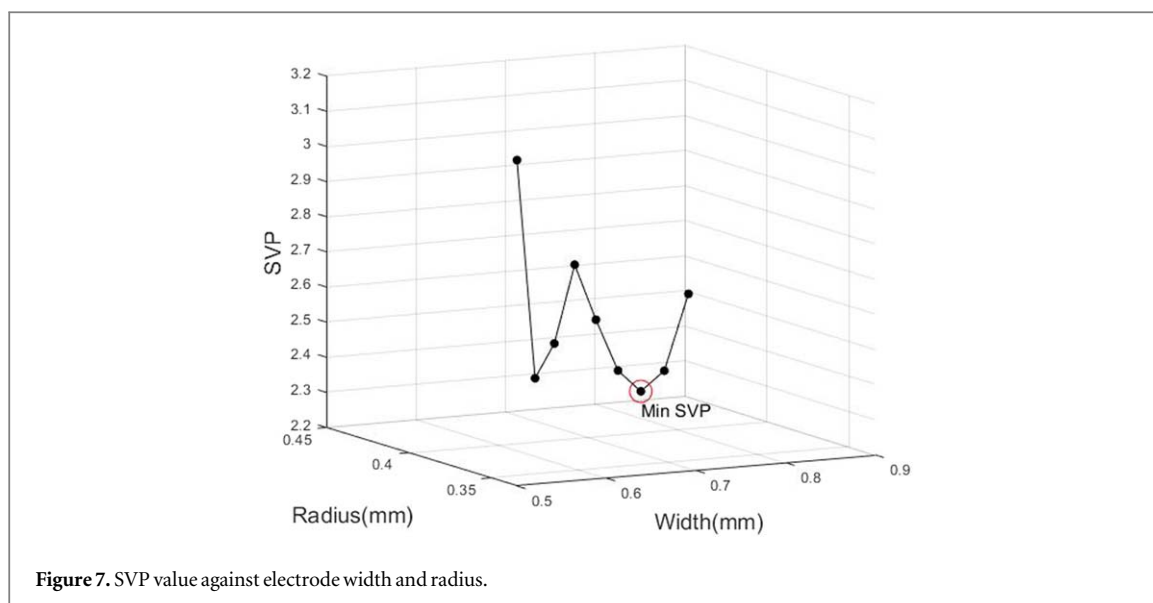
$$wl = 2\pi r^2 \quad (13)$$

$$r = \sqrt{\frac{wl}{2\pi}} \quad (14)$$

where C is the capacitance, ε is the permittivity, A is the area of the electrode, d is the distance between electrodes, w is the width of the peripheral electrode, l is the length of the peripheral electrode, and r is the radius of central electrode. Thus, as formulated in equation (14), the radius of the central electrode is alternated according to the width of the peripheral electrode. A series of peripheral electrode widths from 0.50 mm to 0.90 mm, with a 0.05 mm step size, were investigated. Meanwhile, the radius of the central electrode is varied according to the electrode width, as defined in equation (14). The SVP result is plotted in figure 7.

According to the graph plotted in figure 7, the peripheral electrode width of 0.8 mm had the smallest SVP value. The central electrode radius corresponds to the 0.8 mm peripheral electrode width is 0.42 mm. Considering the ease of fabrication, 0.4 mm is chosen as the radius of the central electrode. The finalized design with the dimensions optimized by the SVP is shown in figure 8.

To validate the impact of using SVP evaluation for optimizing the electrode dimension, the imaging performance of the finalized design in figure 8 is compared quantitatively with the configuration IV in figure 3. Their performances are evaluated by placing a cubic imaging object at different locations as shown in figure 4. The comparison result of the correlation coefficient is plotted in figure 9. The results show the finalized design had poorer performance at positions P1 and P3 with lower correlation coefficient values. Nevertheless, the finalized design performed better in other locations. On the other hand, according to the correlation coefficient tabulated in table 3, the finalized design demonstrated better performance over the previous design with a higher average correlation coefficient of 0.5380. The SVP evaluation aims to provide a guideline in defining the electrode dimension in the electrode design.



3.3. Volumetric shapes restoration for the finalized electrode design

In this section, the performance of the finalized design in restoring different volumetric shapes is evaluated. The shapes used for the evaluation were cube, cylinder, pyramid, and sphere. Results in table 4 show that the finalized design could not differentiate the shapes, in which the reconstructed shapes were alike to each other. This is because the number of capacitance measurements is less than the number of pixels. Compared to two-dimensional imaging, three-dimensional imaging faces a more severe underdetermined problem, as it needs to solve a larger domain with a limited number of measurements. Besides electrode number, electrode placement is also critical for shape restoration, as the electrode placement influences the projection angle of the electric field between an electrode pair. Thus, increasing the electrode number with proper placement may succeed in the shape restoration. The results show that, even though the finalized design failed to restore the shape perfectly, the system manage to distinguish all the positions of the imaging object in a three-dimensional space despite the shape difference.

4. Experimental study

As illustrated in figure 10, the electrode design, which consists of 16 peripheral electrodes and the central electrode, is printed on a printed circuit board (PCB) following the optimized dimension in figure 8. The electrode surface is finished by a layer of nickel and gold to withstand the corrosion. The PCB thickness is 1.6 mm, and the copper weight is 1 Ounce. Total of two PCB plates are printed, one for the top electrode plate, and another for the bottom electrode plate. The bottom electrode plate is bonded to the polydimethylsiloxane (PDMS) microchamber by coating a thin layer of prepolymer mixture between their bonding area. During the

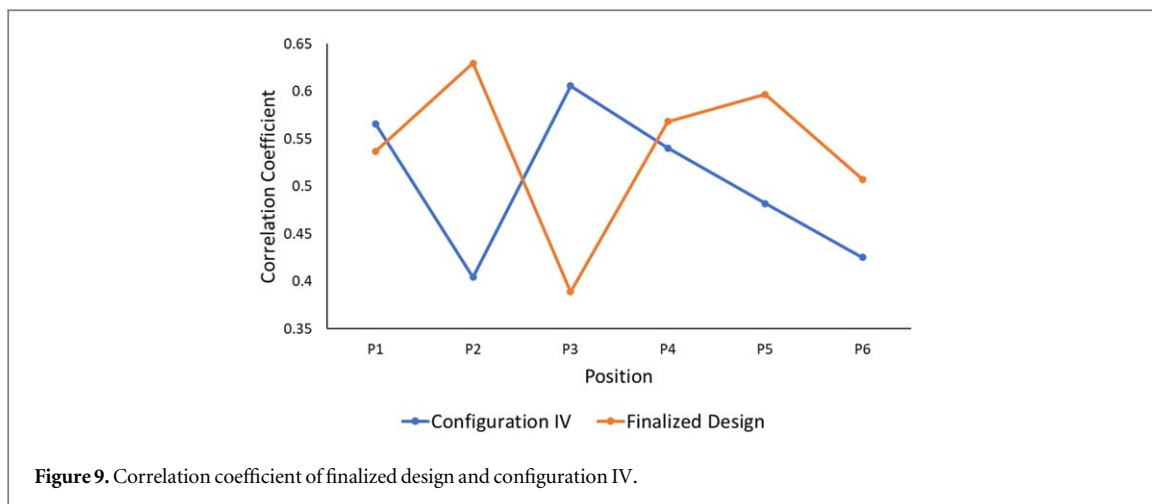
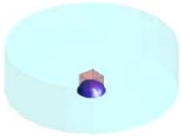
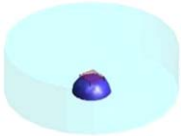

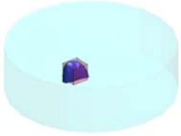
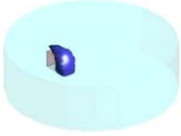
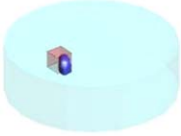


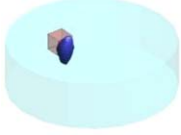
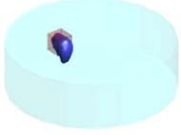
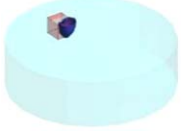
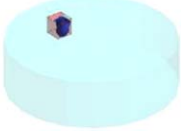


Figure 9. Correlation coefficient of finalized design and configuration IV.

Table 3. Correlation coefficient of configuration IV and finalized design.

Position	Correlation Coefficient	
	Configuration IV (Refer to Figure 3)	Finalized Design (Refer to Figure 8)
P1	 0.5657	 0.5371
P2	 0.4042	 0.6298
P3	 0.6057	 0.3888
P4	 0.5403	 0.5682
P5	 0.4819	 0.5969
P6	 0.4251	 0.5074
AVERAGE	0.5038	0.5380

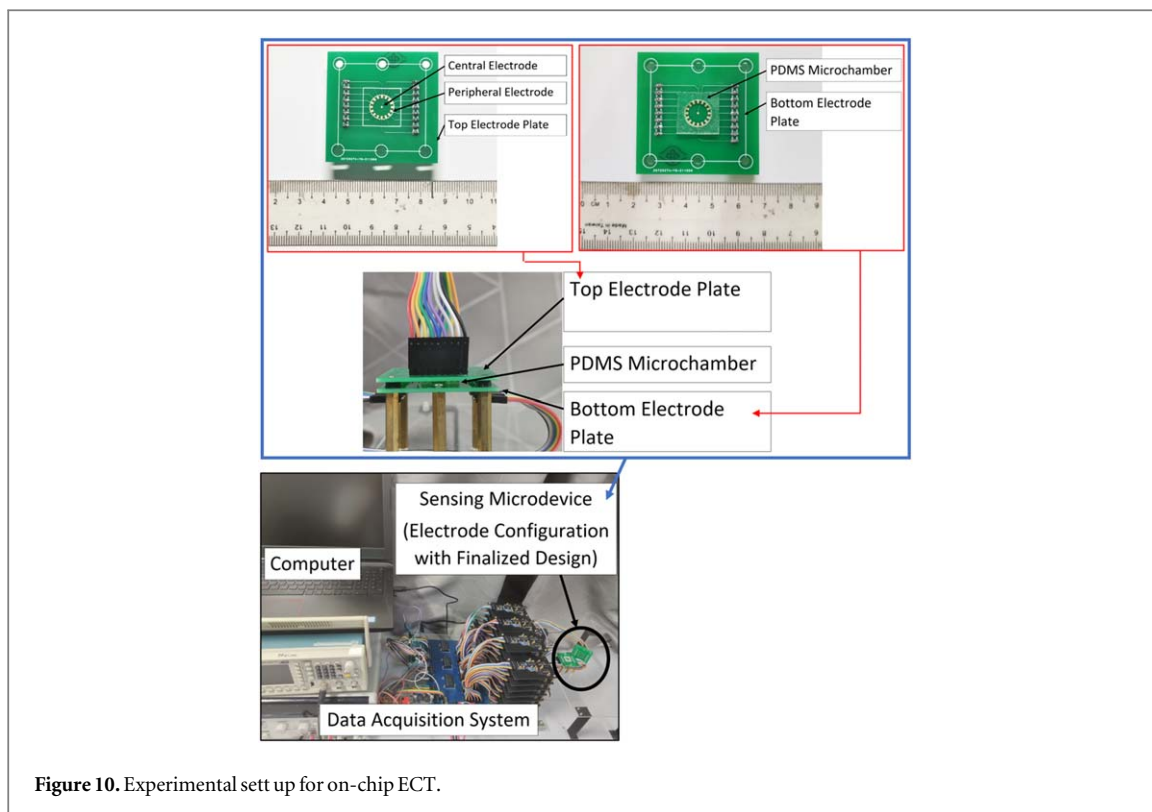
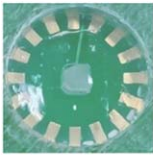
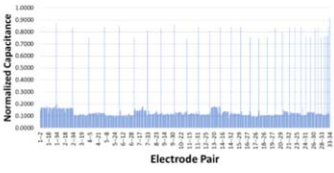
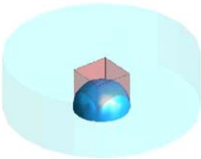
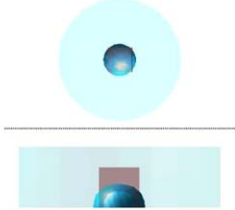
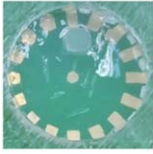
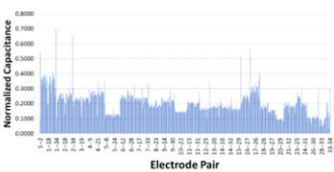
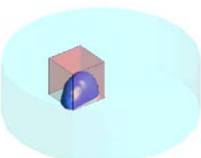

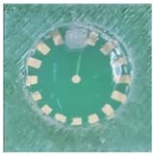
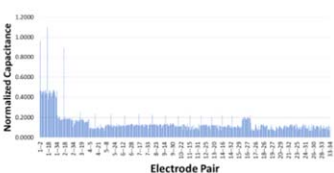
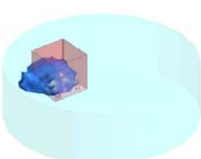
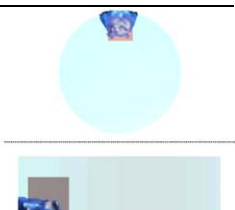
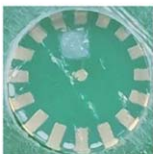
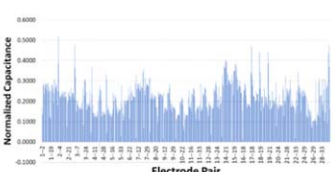
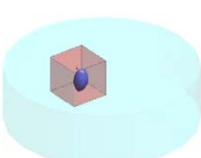

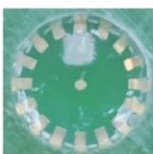
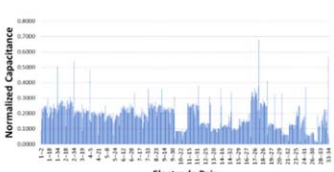
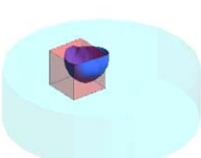
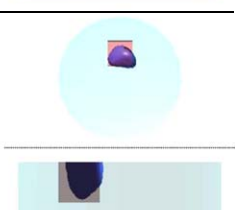


Figure 10. Experimental sett up for on-chip ECT.

Table 4. Simulation results of different volumetric shapes.

Position	Cube	Cylinder	Pyramid	Sphere
P1				
P2				
P3				
P4				
P5				
P6				

Table 5. Experimental results.

Position	Experimental Model (Top View)	Normalized Capacitance	Reconstructed Image	
			Isometric View	Top View /Side View
P1				
P2				
P3				
P4				
P5				

measurement, the PDMS microchamber is enclosed with the top electrode plate. The round sensing region of the PDMS microchamber is 3 mm in height and 10 mm in diameter, which is same as the previous simulation study.

As depicted in figure 10, the 34 planar electrodes were connected to their respective measuring channels of the data acquisition system. The data acquisition system was developed based on the AC-based measuring method proposed by [6], in which the output voltage is directly proportional to the measured capacitance. The details in developing the data acquisition system for this work is included in [21]. The result of taking measurement across different frequencies of 100 Hz, 120 Hz, 1 kHz, 10 kHz, and 100 kHz with the Keysight Agilent U1733C LCR meter is plotted in figure 13. Referring figures 13, 10 kHz was the measuring frequency because the imaging samples of *Saccharomyces Cerevisiae* show the most capacitive characteristic of -54° phase angle at 10 kHz. Whereas, the measuring range was up to 10 nF with some tolerance, as the capacitance of an adjacent electrode pair was 934 pF at 10 kHz when the PDMS microchamber was fully filled with the imaging samples [21]. The capacitance was in pF order as the planar electrodes were uncoated with any insulating layer of PDMS or glass. The capacitance would decrease down to fF order if the electrodes were coated with an insulating

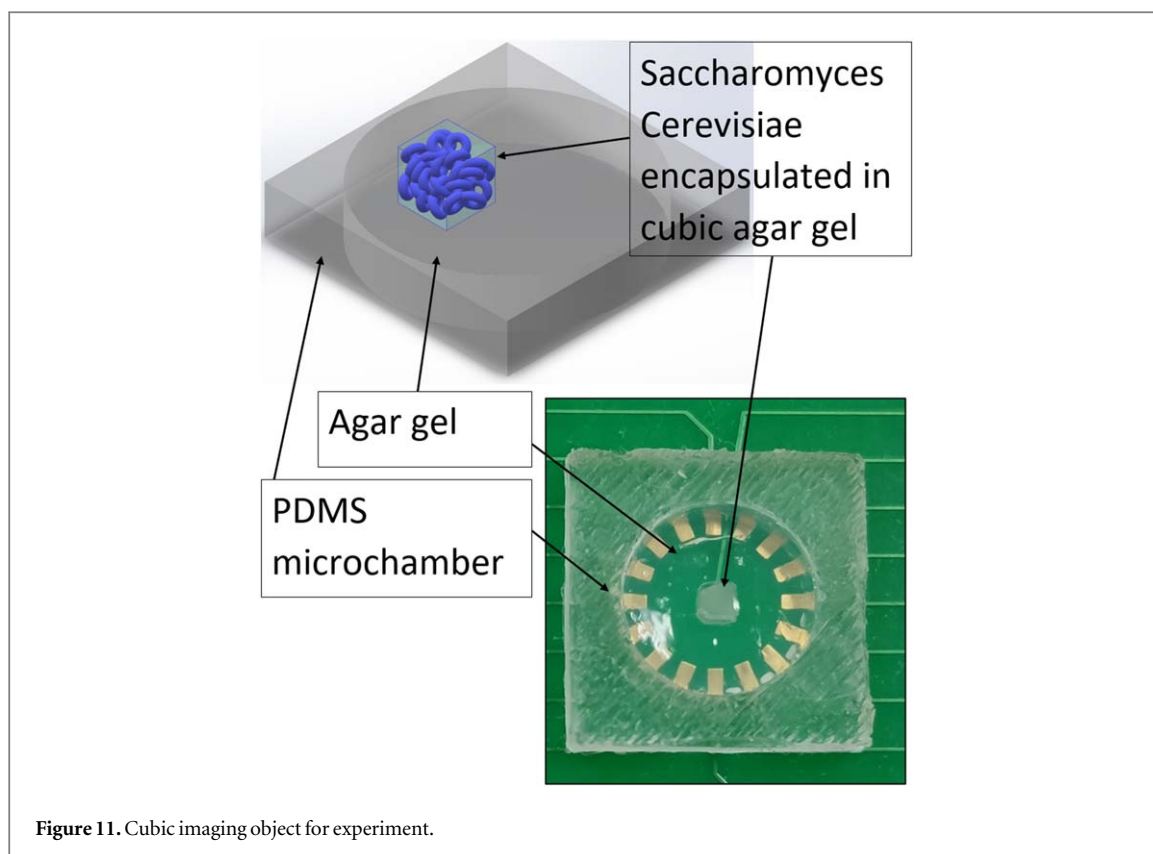


Figure 11. Cubic imaging object for experiment.

layer. The relative error of the data acquisition system was 6% for capacitance value higher than 10 pF with the maximum standard deviation of 7.37 pF [21]. The collected capacitance signals were transferred by the data acquisition system to the computer for image reconstruction via an universal serial bus (USB) cable.

The cubic imaging object was created by encapsulating the *Saccharomyces Cerevisiae* (a type of yeast) within a cubic agar gel, as shown in figure 11. Whereas, the rest of the PDMS microchamber sensing region was filled with the agar gel serving as the background medium. Due to polarization, the yeast cells encapsulated within agar gel demonstrates higher capacitive property than the pure agar gel itself [27]. Agar gel is a bioactive and biocompatible material that is used for culturing cells in three-dimensions [28, 29]. The size of the cubic imaging object was 2 mm. The capacitance changes of the pF order is induced in the experiment as the 2 mm cubic imaging object is close to the electrodes and relatively big in the microchamber. The length and height ratio of the imaging object and the microchamber are 20% and 67%, respectively. During the experiment, the cubic imaging object was placed across five different positions shown in figure 12 to examine the three-dimensional imaging ability of the designed electrode configuration.

The imaging results is tabulated in table 5. The outline of the exact cubic imaging object is hardly restored. However the imaging object at all the five positions was located successfully using the dual electrode plates design. To better evaluate the imaging performance, the reconstructed images are plotted against their respective correlation coefficient in figure 14. The trend reveals that, by using the design of the peripheral and central electrodes in practice, the quality of reconstruct image decreased quantitatively when the imaging object was away from the central region, position P1 and moving towards the peripheral region, position P3. The performance was the weakest when the imaging object was floating in the microchamber at position P4. Due to the less significant trend of normalized capacitance, the image quality at the position P4 was less satisfactory with the correlation coefficient of 0.1880. However, the location of the imaging object was still restored successfully. Whereas, the imaging object at the top of the microchamber, position P5 was successfully reconstructed with the correlation coefficient higher than 0.4600, by employing the top electrode plate. Overall, the performance in experiment was fairly good with an average correlation coefficient of 0.4370. The experimental success indicated that using the proposed electrode configuration (dual sensing planes design) to reconstruct the images of the micro-platform in three-dimensions was practical. The desired electrode configuration could be realized by sandwiching the microchamber between two electrode plates, which consisted of the peripheral and central electrode.

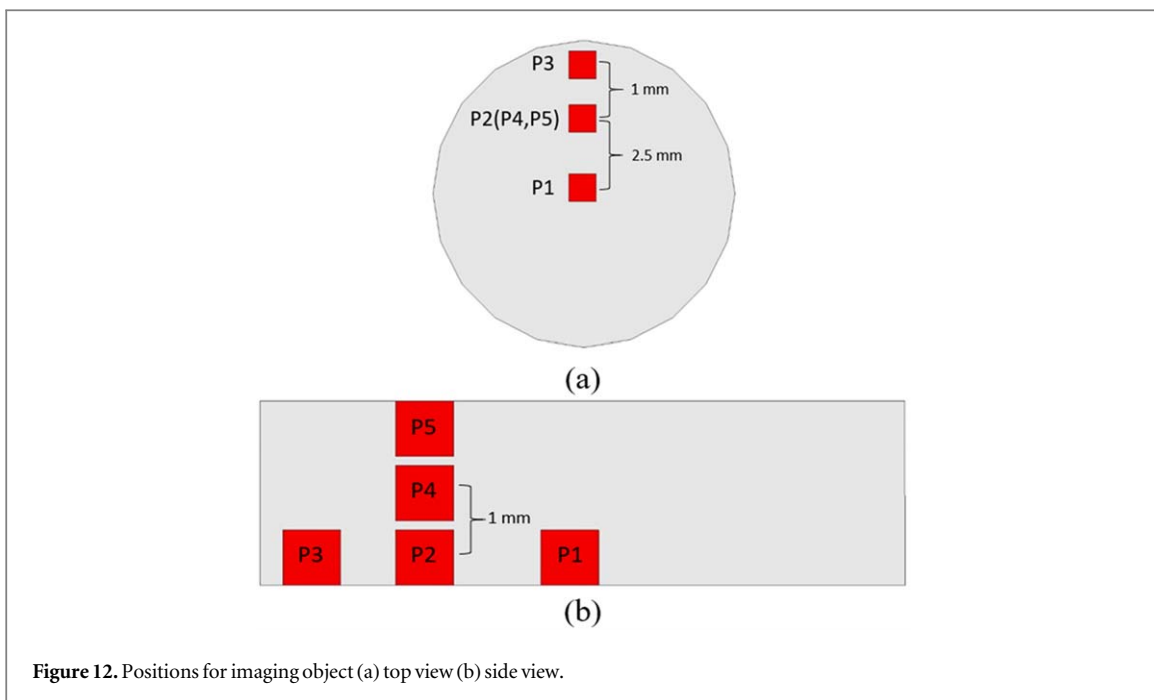


Figure 12. Positions for imaging object (a) top view (b) side view.

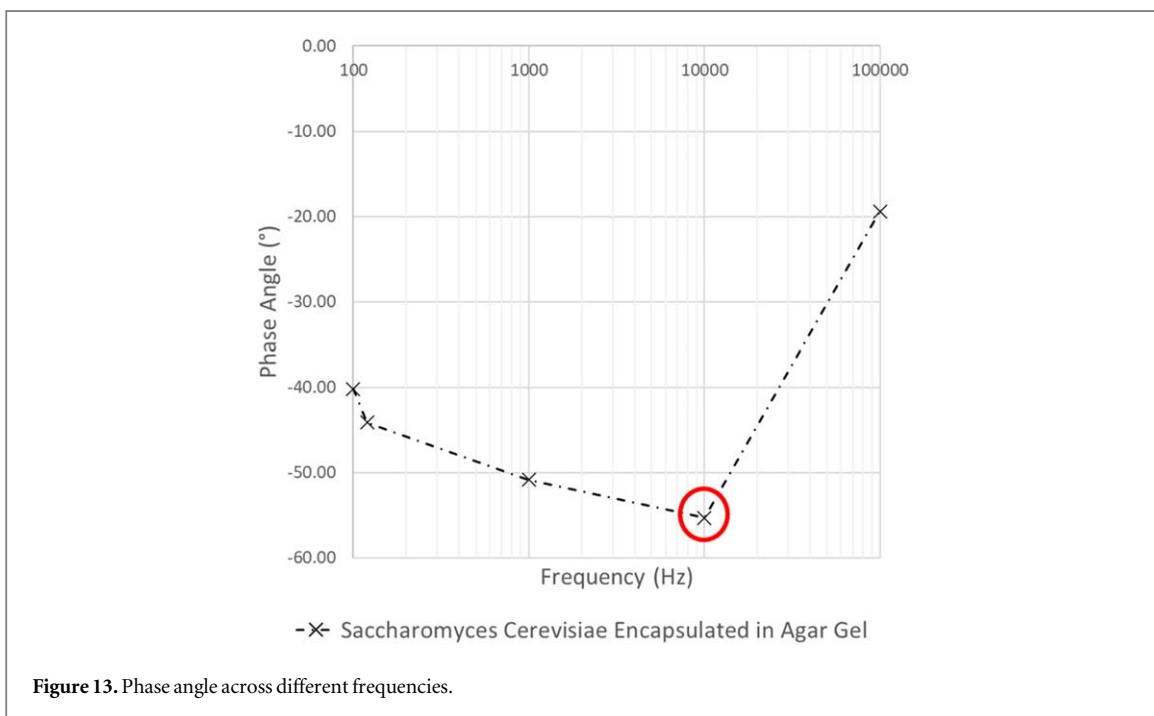


Figure 13. Phase angle across different frequencies.

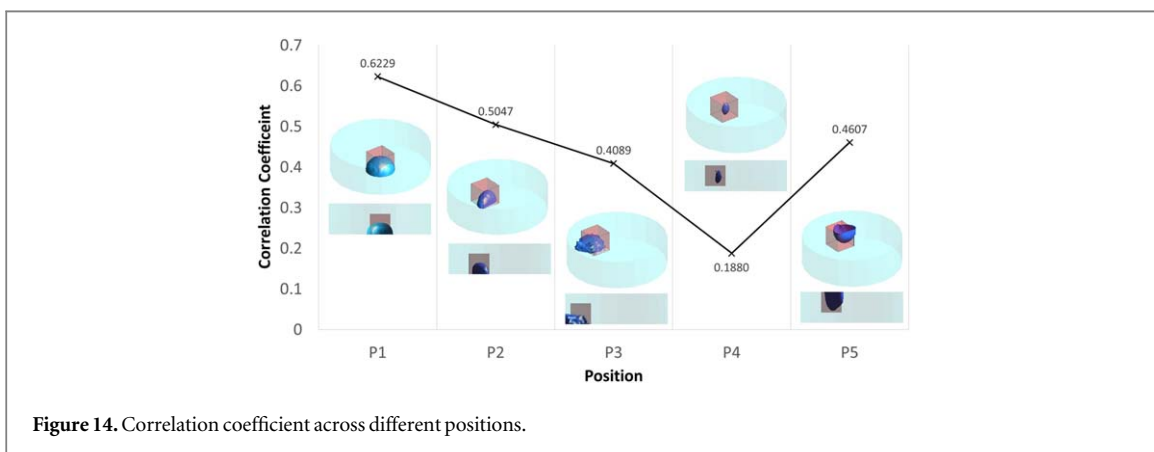


Figure 14. Correlation coefficient across different positions.

5. Conclusion

This work has demonstrated a series of simulation and experimental study on the electrode design of an on-chip ECT for three-dimensional imaging. The results show the electrode configuration IV, which was equipped with two sensing planes, successfully reconstructed the imaging object at different positions. Each sensing plane was equipped with 16 peripheral electrodes and a central electrode to generate a uniform sensitivity distribution. The central electrode is crucial to strengthen the sensitivity at the center area of the sensing region. Without the central electrode, the floating object cannot be restored. In addition, the comparison result suggests that the SVP parameter is suitable for guiding the electrode dimension, as the optimized dimension performed better with a higher average correlation coefficient of 0.5380. Despite the SVP guidance, the electrode dimension can be increased to capture the capacitance changes induced by smaller imaging object in the practice of the future work. Nonetheless, due to the underdetermined equations that cause the ill-posed inverse problem, the proposed electrode configuration failed to distinguish the shape of the imaging object. The experiment has verified the viability of employing dual sensing planes in practice to achieve the three-dimensional imaging on a micro-platform. The overall results prove that an on-chip ECT can locate an imaging object in three-dimensions with an appropriate electrode configuration. The development of on-chip ECT further enrich the lab-on-chip application in handling the samples on a micro-platform by providing the three-dimensional imaging. The samples could be flowing fluids [15] or cell culture [21], which present permittivity difference from the background. For the future work, advanced image reconstruction algorithms can be applied to further study the potential and limit of the suggested electrode configuration.

Acknowledgments

This work was supported by Universiti Teknologi Malaysia [Q. J130000.2451.04G93, Q. J130000.2551.20H93]; and the Ministry of Higher Education Malaysia [FRGS/1/2020/TK0/UTM/02/47].

Data availability statement

All data that support the findings of this study are included within the article (and any supplementary files).

Conflicts of interest

The authors declare no conflict of interest.

ORCID iDs

Xian Feng Hor  <https://orcid.org/0000-0002-6076-0525>

Pei Ling Leow  <https://orcid.org/0000-0001-7930-4717>

Mohamed Sultan Mohamed Ali  <https://orcid.org/0000-0002-4692-2954>

Pei Song Chee  <https://orcid.org/0000-0001-7165-7788>

Shahrulnizahani Mohammad Din  <https://orcid.org/0000-0003-3237-5336>

Wen Pin Gooi  <https://orcid.org/0000-0001-7635-2334>

References

- [1] Waterfall R C 2000 Imaging combustion using electrical capacitance tomography *IEE Colloq.* **80** 57–60
- [2] Mohamad E J, Rahim R A, Rahiman M H F, Ameran H L M, Muji S Z M and Marwah O M F 2016 Measurement and analysis of water/oil multiphase flow using electrical capacitance tomography sensor *Flow Meas Instrum [Internet]*. **47** 62–70
- [3] Perera K, Pradeep C, Mylvaganam S and Time R W 2017 Imaging of oil-water flow patterns by electrical capacitance tomography *Flow Meas Instrum [Internet]*. **56** 23–34
- [4] Wang H and Yang W 2021 Application of electrical capacitance tomography in pharmaceutical fluidised beds—a review. *Chem Eng Sci [Internet]*. **231** 116236
- [5] Gamio C, Ortiz-Aleman J, Martin C and Elctrical R 2005 Capacitance tomography two-phase oil-gas pipe flow imaging by the linear back-projection algorithm *Geofis Intenational [Internet]*. **44** 265–73
- [6] Yang W Q and York T A 1999 New AC-based capacitance tomography system *IEE Proc - Sci Meas Technol [Internet]*. **146** 47–53
- [7] Yang W Q and Peng L 2003 Image reconstruction algorithms for electrical capacitance tomography *Meas Sci Technol [Internet]*. **14** R1–13
- [8] Li K and Cong S 2018 A review of image reconstruction algorithms in electrical capacitance tomography *Tenth Int. Conf. on Advanced Computational Intelligence (ICACI) [Internet]*. *IEEE*; **2018** 128–33

- [9] Yanli G, Qing X, Kunming L and Junjie G 2018 37 Overview on image reconstruction algorithms for electrical capacitance tomography *th Chinese Control Conf. (CCC) [Internet]. IEEE* **2018** 3405–11
- [10] Yang W 2010 Design of electrical capacitance tomography sensors *Meas. Sci. Technol.* **21** 4
- [11] Warsito W, Marashdeh Q and Fan L-S 2007 Electrical capacitance volume tomography *IEEE Sens J [Internet].* **7** 525–35
- [12] Yan H, Wang Y F and Zhou Y G 2011 Research on direct 3D ECT imaging: sensor modeling and image reconstruction *Int. Conf. on Computational and Information Sciences [Internet]. IEEE; 2011.* pp 95–8
- [13] Sun T, Tsuda S, Zauner K-P and Morgan H 2010 On-chip electrical impedance tomography for imaging biological cells *Biosens Bioelectron [Internet].* **25** 1109–15
- [14] Sun T, Tsuda S, Zauner K-P and Morgan H 2009 Single cell imaging using electrical impedance tomography *4th IEEE Int. Conf. on Nano/Micro Engineered and Molecular Systems [Internet]. IEEE; 2009.* pp 858–63
- [15] Mohammad Din S et al 2018 Planar imaging of stagnant and hydrodynamic fluid using miniaturized ECT Device *Int J Integr Eng [Internet].* **10** 131–5
- [16] Yin X, Wu H, Jia J and Yang Y 2018 A micro EIT sensor for real-time and non-destructive 3D cultivated cell imaging *IEEE Sens J [Internet].* **18** 5402–12
- [17] Rahman A R A, Register J, Vuppala G and Bhansali S 2008 Cell culture monitoring by impedance mapping using a multielectrode scanning impedance spectroscopy system (CellMap) *Physiol Meas [Internet].* **29** S227–39
- [18] Linderholm P, Braschler T, Vannod J, Barrandon Y, Brouard M and Renaud P 2006 Two-dimensional impedance imaging of cell migration and epithelial stratification *Lab Chip* **6** 1155–62
- [19] Linderholm P, Vannod J, Barrandon Y and Renaud P 2007 Bipolar resistivity profiling of 3D tissue culture *Biosens. Bioelectron.* **22** 789–96
- [20] Linderholm P, Marescot L, Loke M H and Renaud P 2008 Cell culture imaging using microimpedance tomography *IEEE Trans. Biomed. Eng.* **55** 138–46
- [21] Hor X F, Leow P L, Mohamed Ali M S, Gooi W P and Mohammad Din S 2022 3D tomogram using on-chip ECT with AC-based capacitance measuring system. control instrum mechatronics theory pract lect notes *Electr Eng [Internet].* **921** 717–28
- [22] Kowalska A, Banasiak R, Wajman R, Romanowski A and Sankowski D 2018 Towards high precision electrical capacitance tomography multilayer sensor structure using 3D modelling and 3D printing method *International Interdisciplinary PhD Workshop (IIPhDW) [Internet]. IEEE; 2018* 238–43
- [23] Din S and Binti M 2019 Electrical potential study of single and segmented excitation for planar electrical capacitance tomography *Icset* **2019** 3–8
- [24] Ramli M F, Tian W and Yang W 2016 Image reconstruction with different sensitivity maps generated with different background *IEEE Int. Conf. on Imaging Systems and Techniques (IST) [Internet]. IEEE* **2016** 543–8
- [25] Yang Y, Jia J, Smith S, Jamil N, Gamal W and Bagnaninchi P-O 2017 A miniature electrical impedance tomography sensor and 3d image reconstruction for cell imaging *IEEE Sens J [Internet].* **17** 514–23
- [26] Xie C G, Stott A L, Plaskowski A and Beck M S 1990 Design of capacitance electrodes for concentration measurement of two-phase flow *Meas. Sci. Technol.* **1** 65–78
- [27] Al Ahmad M, Al Natour Z, Attoub S and Hassan A H 2018 Monitoring of the budding yeast cell cycle using electrical parameters *IEEE Access.* **6** 19231–7
- [28] Bao M, Xie J and Huck W T S 2018 Recent advances in engineering the stem cell microniche in 3D *Adv. Sci.* **5** 8
- [29] Napolitano A P et al 2007 Scaffold-free three-dimensional cell culture utilizing micromolded nonadhesive hydrogels *Biotechniques.* **43** 494–500